Numerical prediction of the Flame Describing Function and thermoacoustic limit cycle for a pressurised gas turbine combustor

Yu Xia and Davide Laera and W. P. Jones and Aimee S. Morgans

Department of Mechanical Engineering, Imperial College London, London SW7 2AZ, U.K.

ABSTRACT

The forced flame responses in a pressurised gas turbine combustor are predicted using numerical reacting flow simulations. Two incompressible[1] LES solvers are used, applying two combustion models and two reaction schemes (4-step and 15-step) at two operating pressures (3 bar and 6 bar). Although the combustor flow field is little affected by these factors, the flame length and heat release rate are found to depend on combustion model, reaction scheme and combustor pressure. The flame responses to an upstream velocity perturbation are used to construct the flame describing functions (FDFs). The FDFs exhibit smaller dependence on the combustion model and reaction chemistry than the flame shape and mean heat release rate. The FDFs are validated by predicting combustor thermoacoustic stability at 3 bar and 6 bar and, for the unstable 6 bar case, also by predicting the frequency and oscillation amplitude of the resulting limit cycle oscillation. All of these numerical predictions are in very good agreement with experimental measurements.

Corresponding author: Yu Xia, Email: yu.xia13@imperial.ac.uk

[1]Incompressible does not imply constant density but rather that the density is independent of pressure variations throughout the flow, i.e. not able to be compressed.

1. Introduction

Numerical prediction of thermoacoustic instability in gas turbine combustors is an ongoing challenge. Many approaches rely on a model for the flame heat release rate response (denoted $\dot{q}$) to velocity perturbation just upstream of the flame (denoted u_1), e.g., Li and Morgans (2015); Han et al. (2015), such as the weakly nonlinear flame describing function (FDF, denoted $\mathcal{F}$), whose gain, G, and phase, φ, depend on the amplitude, $|\widehat{u}_1/\overline{u}_1|$, and frequency, ω, of the perturbation as (Noiray et al., 2008):

$$\mathcal{F}\left(\omega, |\widehat{u}_1/\overline{u}_1|\right) = \frac{\widehat{\dot{q}}/\overline{\dot{q}}}{\widehat{u}_1/\overline{u}_1} = G\left(\omega, |\widehat{u}_1/\overline{u}_1|\right)\exp\left(i\varphi\left(\omega, |\widehat{u}_1/\overline{u}_1|\right)\right), \tag{1}$$

where $\widehat{(\cdot)}$ denotes amplitude fluctuations in the frequency domain, and $\overline{(\cdot)}$ the time-averaged quantities.

Many numerical simulations of premixed flame FDFs use fully compressible large eddy simulations (LES), e.g., Krediet et al. (2013); Lee and Cant (2017). However, the computational costs are extremely large due to the very small time step limited by the inverse of speed of sound. Recently, the fact that the flame primarily responds to hydrodynamic disturbances (originally excited by the acoustics) has been exploited by using incompressible LES (Febrer et al., 2011; Han & Morgans, 2015): the convective flow speed rather than the speed of sound then determines the time step and thus allows much larger values, making incompressible simulations significantly faster than fully compressible ones. With this approach, a complete FDF for a premixed bluff-body stabilised flame was accurately predicted (Han et al., 2015), as were the nonlinear FDFs of a swirling premixed flame (Xia, Morgans, Jones, & Han, 2017) and a very long non-swirling flame (Xia, Li, et al., 2017; Li et al., 2017) and, recently, the linear flame response of a stratified flame (Han et al., 2018), etc.

In most flame LES studies, the chemical reaction is modelled by a simplified scheme involving only a few reaction steps, e.g., Han et al. (2015); Bauerheim et al. (2015). Although the impact of reaction chemistry on an unforced methane flame was recently investigated (Fedina

et al., 2017), to the authors' knowledge there is no similar study for a forced flame, where an accurate reproduction of the flame response is vital for FDF prediction. This is even more important when the operating pressure is high. Very few LES cases have considered an unforced flame (Bulat et al., 2014) or linear flame response (Hermeth et al., 2014) at elevated pressures, representative of real combustor operations, but none thus far have realistically accounted for the nonlinear forced flame response at such high pressures.

The present work thus aims to numerically simulate the nonlinear flame response in a pressurised realistic combustor, using incompressible LES. The effects of sub-grid combustion models, reaction schemes, and operating pressures on the flame shape and the FDFs are analysed. In order to validate the computed FDFs, thermoacoustic predictions are performed by combining with a low order network approach for the acoustic waves.

2. Mathematical Formulation of Incompressible LES

The filtered conservation equations of mass, momentum, species mass fractions and enthalpy solved by the incompressible LES are:

$$
\begin{cases}
\dfrac{\partial \overline{\rho}}{\partial t} + \dfrac{\partial \overline{\rho}\widetilde{u}_i}{\partial x_i} = 0, & \text{(2a)} \\[3mm]
\dfrac{\partial \overline{\rho}\widetilde{u}_i}{\partial t} + \dfrac{\partial \overline{\rho}\widetilde{u}_i\widetilde{u}_j}{\partial x_j} = -\dfrac{\partial \overline{p}}{\partial x_i} + \dfrac{\partial}{\partial x_j}\left(\overline{\mu}\left[\dfrac{\partial \overline{u}_i}{\partial x_j} + \dfrac{\partial \overline{u}_j}{\partial x_i}\right]\right) - \dfrac{\partial}{\partial x_j}\tau_{\mathrm{ij}}, & \text{(2b)} \\[3mm]
\dfrac{\partial \overline{\rho}\widetilde{Y}_\alpha}{\partial t} + \dfrac{\partial \overline{\rho}\widetilde{u}_i\widetilde{Y}_\alpha}{\partial x_i} = \dfrac{\partial}{\partial x_i}\left(\dfrac{\overline{\mu}}{\sigma_m}\dfrac{\partial \overline{Y}_\alpha}{\partial x_i}\right) - \dfrac{\partial J_{\alpha,i}}{\partial x_i} + \overline{\rho}\widetilde{\dot{\omega}}_\alpha, & \text{(2c)} \\[3mm]
\dfrac{\partial \overline{\rho}\widetilde{h}}{\partial t} + \dfrac{\partial \overline{\rho}\widetilde{u}_i\widetilde{h}}{\partial x_i} = \dfrac{\partial}{\partial x_i}\left(\dfrac{\overline{\mu}}{\sigma_m}\dfrac{\partial \overline{h}}{\partial x_i}\right) - \dfrac{\partial J_{h,i}}{\partial x_i}, & \text{(2d)}
\end{cases}
$$

where $\widetilde{()}$ denotes density-weighted filtering, ρ density, u velocity, p pressure, h enthalpy (including the enthalpy of formation), μ dynamic viscosity and σ_m the Prandtl or Schmidt number as appropriate, with the latter assumed the same for all the species. The Lewis number, Le, is assumed unity, so that the Prandtl and Schmidt numbers are equal, implying Fourier heat conduction and Fickian diffusion. The equation of state used is the ideal gas equation, $\rho = \frac{P_0 W_g}{RT}$,

with R the universal gas constant, W_g the molar mass of the mixture, T the temperature and P_0 the constant operating pressure. The temperature and heat release rates are computed as a function of enthalpy and composition using JANAF data (National Institute of Standards and Technology (NIST), 1998). $J_{\alpha,i}$ and $J_{h,i}$ are the sub-grid scalar fluxes for the α-th species (with $\alpha = [1, \cdots, N_{\text{sp}}]$ and N_{sp} the total number of species) and the enthalpy, h, respectively, both modelled by the sub-grid eddy viscosity, μ_{sgs}. $\tau_{\text{ij}} = \overline{\rho} \left(\widetilde{u_i u_j} - \widetilde{u}_i \widetilde{u}_j \right)$ is the sub-grid stress tensor, and $\widetilde{\dot{\omega}}_\alpha = \widetilde{\dot{\omega}}(Y_\alpha)$ the filtered chemical reaction rate, with Y_α the species mass fraction.

In order to model the unknown stress, τ_{ij}, the dynamic Smagorinsky model (Piomelli & Liu, 1995) is applied, which has been found to offer sufficient accuracy. For the filtered term, $\widetilde{\dot{\omega}}_\alpha$, two models are applied: (i) the probability density function (PDF) model (Jones & Navarro-Martinez, 2007; Jones & Prasad, 2010), and (ii) the partially stirred reactor (PaSR) model (Sabelnikov & Fureby, 2013). In the former case, Eqs. (2c) and (2d) are not solved directly, but rather the spatially filtered joint PDF, $\widetilde{P}_{\text{sgs}}$, for all the relevant scalars (e.g., the species mass fractions and enthalpy) is used:

$$
\begin{aligned}
&\overline{\rho} \frac{\partial \widetilde{P}_{\text{sgs}}\left(\underline{\psi}\right)}{\partial t} + \overline{\rho} \widetilde{u}_j \frac{\partial \widetilde{P}_{\text{sgs}}\left(\underline{\psi}\right)}{\partial x_j} + \sum_{\alpha=1}^{N_s} \frac{\partial}{\partial \psi_\alpha} \left[\overline{\rho} \dot{\omega}_\alpha \left(\underline{\psi}\right) \widetilde{P}_{\text{sgs}}\left(\underline{\psi}\right) \right] = \\
&\frac{\partial}{\partial x_i} \left[\left(\frac{\mu}{\sigma_m} + \frac{\mu_{\text{sgs}}}{\sigma_{\text{sgs}}} \right) \frac{\partial \widetilde{P}_{\text{sgs}}\left(\underline{\psi}\right)}{\partial x_i} \right] - \frac{\overline{\rho} C_d}{2 \tau_{\text{sgs}}} \sum_{\alpha=1}^{N_s} \frac{\partial}{\partial \psi_\alpha} \left[(\psi_\alpha - \varphi_\alpha(\boldsymbol{x}, t)) \widetilde{P}_{\text{sgs}}\left(\underline{\psi}\right) \right],
\end{aligned}
\tag{3}
$$

where ψ_α is the sample (composition) space of an arbitrary scalar, $\varphi_\alpha(\boldsymbol{x}, t)$, appearing at location $\boldsymbol{x}$ and time t, and $\underline{\psi}$ the global composition of all the involved scalars. The filtered $\widetilde{\dot{\omega}}_\alpha$ now appears as closed in Eq. (3), which is solved by the Eulerian stochastic field method (Jones & Navarro-Martinez, 2007). The joint PDF is represented as an ensemble of stochastic fields. These fields have no direct physical significance, but instead represent an equivalent stochastic system that has the same one-point PDF as that given by Eq. (3). Any filtered scalar can now be obtained by averaging over all the corresponding stochastic fields.

For the PaSR model, a different modelling concept is used. The flow in a mesh cell is divided into two parts: (i) a "perfectly-stirred reactor", where all species are assumed ho-

mogeneously mixed and reacting, and (ii) "surroundings", filling with non-reacting sub-grid scale flow structures. The burnt products from part (i) are mixed with the "surrounding flow" due to turbulence, giving the final species concentrations in the entire, partially-stirred, computational cell (Han et al., 2015). In any cell the reaction only occurs within domain (i). The relative proportions of these two domains are controlled by the reactive volume fraction, $\kappa = \tau_c/(\tau_c + \tau_m)$ (Chomiak & Karlsson, 1996), governed by the chemical reaction time, τ_c, and the turbulent mixing time, τ_m. To compute τ_c, an accurate chemical reaction scheme is needed. Since the accuracy of a reaction scheme generally increases with the number of reaction steps, in this work two schemes with different complexity levels are considered — a 4-step reaction with 7 intermediate species (Abou-Taouk et al., 2016), and a 15-step scheme with 19 species (Sung et al., 2001) — to evaluate the impact of reaction accuracy on the flame behaviour.

The mixing time is defined as $\tau_m = C_m\sqrt{\tau_\Delta \cdot \tau_K}$ (Fureby et al., 2015), where $\tau_\Delta = \Delta/u'_{\mathrm{sgs}}$ denotes the sub-grid mixing time, with Δ the local mesh size and u'_{sgs} the sub-grid scale velocity fluctuation. $\tau_K = \sqrt{\nu/\epsilon_{\mathrm{sgs}}}$ is the Kolmogorov time, with ϵ_{sgs} the sub-grid dissipation rate and ν the molecular kinematic viscosity. The mixing time constant, C_m, is fixed as 0.8. The filtered chemical reaction rate, $\widetilde{\dot{\omega}}_\alpha$, is modelled by κ as (Han et al., 2015):

$$\widetilde{\dot{\omega}}_\alpha \simeq \kappa \cdot \dot{\omega}_\alpha\left(\bar{\rho}, \widetilde{T}, \widetilde{Y}_\beta, C_1^\alpha\right), \quad \text{with} \ \ \beta = 1, 2, \ldots, N_{sp} \tag{4}$$

where C_1 is the concentration of the species that is leaving the mesh cell.

In this work, the PDF model (with one field) is implemented into an incompressible in-house LES code, BOFFIN (Jones et al., 2012), and the PaSR model is used by the incompressible ReactingFOAM-LES solver in the open-source CFD toolbox, OpenFOAM (version 2.3.0) (Weller et al., 1998). Since only one field is used by the PDF model, the resulting PDF reduces to a δ-function (one unique realisation), which is no longer stochastic. Thus the sub-grid scale turbulence-combustion interactions are neglected in the present BOFFIN study.
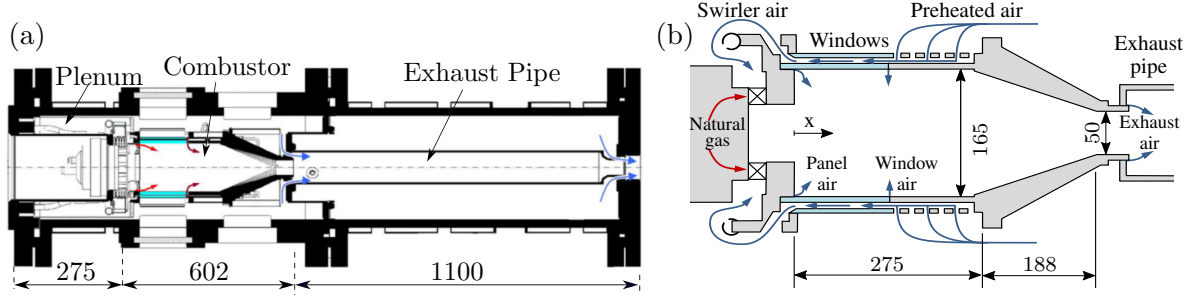
Figure 1. (a) Schematic of the SGT-100 combustor rig; (b) detailed structure of the combustor. All dimensions in mm, with the x-origin located at combustion chamber inlet. Images adapted from Stopper et al. (2010).

3. Experimental Set-up and Numerical Framework

This work studies the pressurised industrial SGT-100 gas turbine combustor. The entire rig (Fig. 1(a)) comprises a swirling combustor, a long exhaust pipe and a spray water section (not shown) connecting to the atmosphere. A cylindrical air plenum upstream of the combustor provides uniform preheated air inflow. The combustor (Fig. 1(b)) consists of a 12-slot radial swirler entry and a premixing chamber, followed by a dump expansion into a $\sim$0.5 m long combustion chamber, which has a straight duct of square cross-section followed by a contraction duct. The exit of the contraction duct is connected to the exhaust pipe via a straight circular pipe. German Natural Gas (Bulat et al., 2014) is injected at temperature 305 K through the swirler entry and mixed with the preheated air at 685 K, reaching a global equivalence ratio of $\varphi = 0.60$ (Stopper et al., 2013). Two operating pressures, $\overline{p} = 3$ bar and 6 bar, are used, with the bulk Reynolds number in the range 18,400 – 120,000 and Mach number in the range 0.02 – 0.29. This combustor has been studied experimentally (Stopper et al., 2010, 2013) at German Aerospace Centre (DLR) and numerically (Bulat et al., 2014; Fedina et al., 2017).

The thermoacoustic stability of the combustor was measured to be dependent on the pressure; being stable at 3 bar, but experiencing limit cycle oscillations at 6 bar (Stopper et al., 2013). Figure 2(a) shows the time-signal of the normalised pressure fluctuation, $p'/\overline{p}$, at 6 bar, measured 231 mm beyond the combustion chamber inlet. The averaged spectrum in Fig. 2(b) exhibits a spectral peak at 216 Hz with amplitude $|\widehat{p}| \simeq 5000$ Pa.
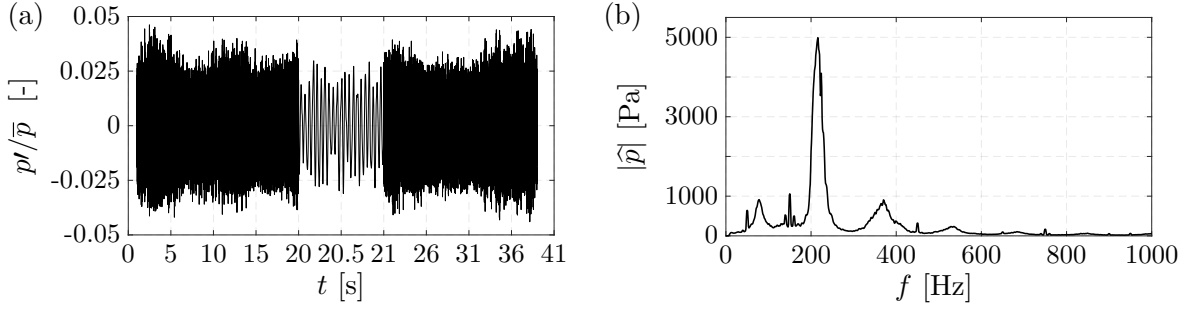
Figure 2. (a) Time-signal of normalised pressure fluctuation, $p'/\overline{p}$, at 6 bar, measured at $x = 231$ mm with a sampling rate of 10 kHz (enlarged time-scale between 20 s and 21 s); (b) Power spectrum of time-signal in (a).

In order to simulate this combustor, we consider a simplified fuel combining all hydrocarbons into methane, giving a composition of 98.97% CH_4, 0.27% CO_2 and 0.753% N_2 (Bulat et al., 2014). The computational domain, shown in Fig. 3(a), neglects the plenum and the exhaust pipe since the flame is restricted to the combustion chamber. A velocity inlet condition consistent with the measured inflow rate is imposed at the swirler entry, including the radial main air inlet and multiple fuel injection holes. The panel air inlet refers to the front edge of the combustion chamber where a small amount of air enters the domain. The outlet corresponds to the combustor exit plane where a zero-gradient and a "non-reflective" outflow condition are applied for pressure and velocity, respectively. Here the "non-reflective" outflow condition is a specific artificial boundary condition, designed to neglect the diffusion effects near the outlet and assumes that the outflow is purely advective (i.e. "non-reflective") (Boström, 2015); it inhibits the occurrence of negative velocities at an outflow boundary. All solid boundaries are defined as non-slip adiabatic walls, consistent with previous LES works on the same combustor (Fedina et al., 2017). The entire domain is discretised with a multi-block structured mesh comprising 7.0 million cells (see Fig. 3(b)), found to be an optimal mesh in a previous study (Bulat, 2012). Mesh refinement is applied to the swirler, premixing chamber and front part of the combustion chamber, to better resolve the flame behaviour.

The numerical schemes used by the present LES are as follows. In BOFFIN a 2nd-order central difference scheme is used for all the spatial discretisations, except for the convective terms in scalar equations where a total variation diminishing (TVD) scheme is used. OpenFOAM

7
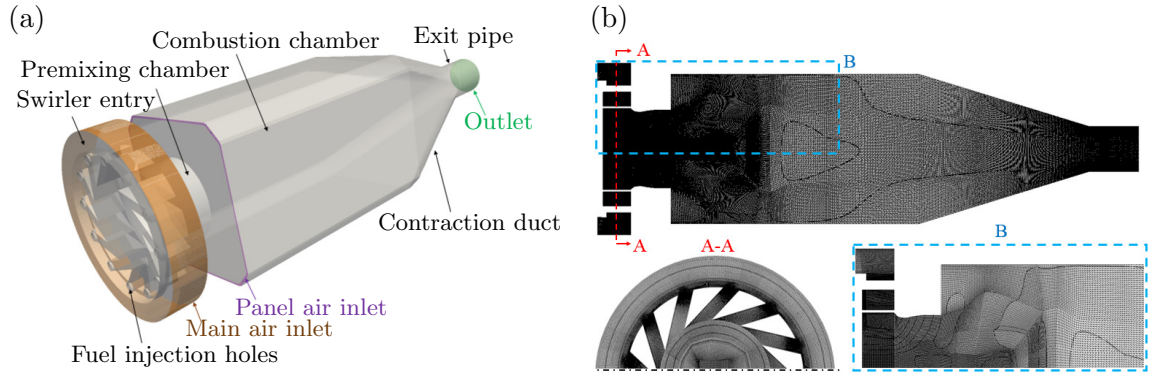
Figure 3. (a) The computational domain (Xia, Duran, et al., 2018) and (b) the optimised 7.0-million-cell multi-block mesh (Bulat, 2012).

Table 1. LES cases used to study the effects of different factors.

Case No.	I	II	III	IV	V
LES solver	OpenFOAM	BOFFIN	BOFFIN	BOFFIN	BOFFIN
Combustion model	PaSR	PDF	PDF	PDF	PDF
Reaction scheme	4-step	4-step	15-step	4-step	15-step
Operating pressure	3 bar	3 bar	3 bar	6 bar	6 bar

adopts a linear Gaussian interpolation scheme for spatial discretisation (which is a central difference method), coupled with a Sweby limiter (Sweby, 1984) improving the stability in regions with rapidly changing gradients but adding numerical diffusivity. Both BOFFIN and OpenFOAM apply an implicit 2nd-order Crank-Nicolson scheme for temporal discretisation. A small fixed time step of 5×10^{-7} s is used to ensure the CFL number is always below 0.3.

4. Unforced LES Results and Validation

The effects of sub-grid combustion model, reaction chemistry and the pressure on the unforced mean flow and flame behaviour are first presented. For systematic comparisons, five LES cases with different modelling assumptions and operating conditions are defined, as listed in Table 1.

The effects of combustion model are investigated by comparing Cases I and II. Figure 4 shows the time-averaged contours of axial velocity, $\overline{u}$, temperature, $\overline{T}$, and volumetric heat release rate, $\overline{\dot{q}}$, on a symmetry plane, with the top-half of each sub-figure referring to Case I

and the bottom-half to Case II. The mean streamlines are superimposed on the contours of $\overline{u}$ and $\overline{T}$ to allow a clear representation of the inner and outer recirculation zones. A central vortex core (CVC) extends along the centreline from the exit to the mid-chamber, with the exit low pressure zone resulting in very high exit velocities on the centreline, dropping off towards the two sides. This CVC has been observed in previous experiments (Stopper et al., 2013) and LES (Bulat et al., 2015; Xia et al., 2016; Xia, Duran, et al., 2018) on the same combustor.

The mean velocity contours are very similar between Cases I and II (Fig. 4(a)), suggesting that the combustion model has negligible effect on the unforced flow field. For the mean temperature and heat release rate fields, however, some discrepancies exist. Case I exhibits a longer low temperature zone and a lower heat release rate. A possible explanation is that OpenFOAM may be more diffusive than BOFFIN, due to its use of a TVD-type scheme for the velocities, which would result in a thicker reaction zone and corresponding lower peak heat release rate. It is also possible that it is a result of the differences in the two combustion models utilised in the two codes.

Figure 5 compares the vertical y-profiles of velocity, temperature and mixture fraction between Cases I and II at four axial locations. The horizontal axis of each sub-figure is thus split into four segments, each refers to a profile and has the same data range for the plotted variable. At $x = 18.7$ mm, very little difference is observed between the PaSR and PDF models for either mean or root-mean-square (rms) velocities, confirming that the combustion model has almost no effect on the flow field. Both cases accurately capture the experimental data. Further downstream ($x \geq 38.7$ mm), good agreement between the LES and experiments is maintained for all velocity profiles, other than for a small mismatch between the two LES cases near the centreline of the v_{rms} profiles (Fig. 5(f)). This may be due to the difference in the CVC's axial length predicted by the two combustion models.

For the temperature, T, both combustion models correctly capture its mean and rms profiles at the first location of $x = 18.7$ mm. Differences between the LES and measurements become
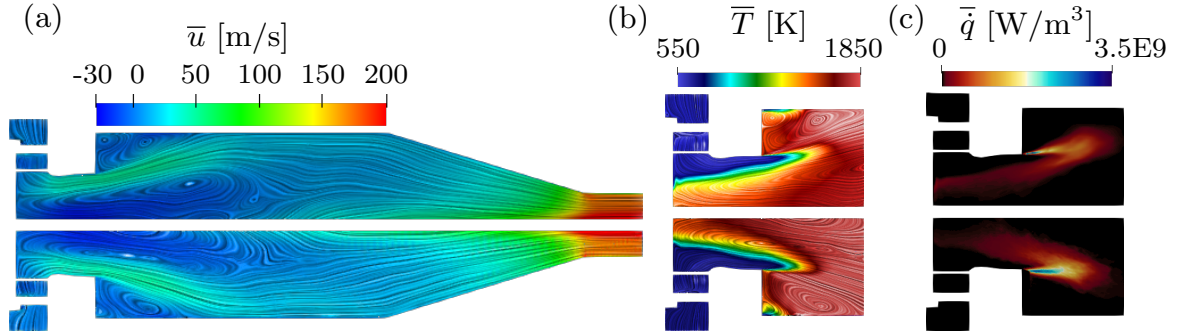
Figure 4. Time-averaged contours of (a) velocity, $\overline{u}$, (b) temperature, $\overline{T}$, and (c) volumetric heat release rate, $\overline{\dot{q}}$, on a symmetry plane, obtained by (top) Case I with PaSR model and (bottom) Case II with PDF model.

more pronounced further downstream. Both LES cases fail to predict the temperature profile near the top wall, although the experimental data here are not complete; and this is consistent with other studies on the same rig (Fedina et al., 2017). Very good agreement is achieved for the mean mixture fraction, $\overline{Z}$, which reveals a globally lean mixture uniformly distributed in the reaction zone. Although small errors exist for z_{rms} profile (Fig. 5(h)), bearing in mind the measurement uncertainties (Bulat et al., 2014), these errors are generally acceptable. It is also noted that the PDF model slightly over-predicts the mean and rms temperature, consistent with the shorter low temperature zone predicted by the same model.

Secondly, the effect of reaction scheme on the unforced LES is studied. To investigate the 4-step and 15-step methane schemes used, their predictions of the laminar burning velocity, S_u, and the adiabatic flame temperature, T_a, are compared to those obtained by a full 325-step GRI-Mech 3.0 scheme (Gregory et al., 2018). The effect of the constant Schmidt and unity Lewis number assumptions is evaluated by comparing the LES predictions of S_u and T_a with those from the chemical solver, Cantera (Goodwin et al., 2014), in which accurate transport properties are used. Figure 6(a) shows calculations performed at $\overline{p} = 3$ bar with an ambient temperature of 650 K, the same conditions as for LES Cases I – III. The Cantera simplified schemes give similar S_u and T_a values to those of the detailed GRI-Mech scheme across a range of equivalence ratios. For the operating point of $\phi = 0.6$, the Cantera 4-step scheme slightly over-predicts the laminar burning velocity, with the 15-step scheme matching better the detailed GRI scheme. The two tested LES solvers slightly under-predict S_u for both the
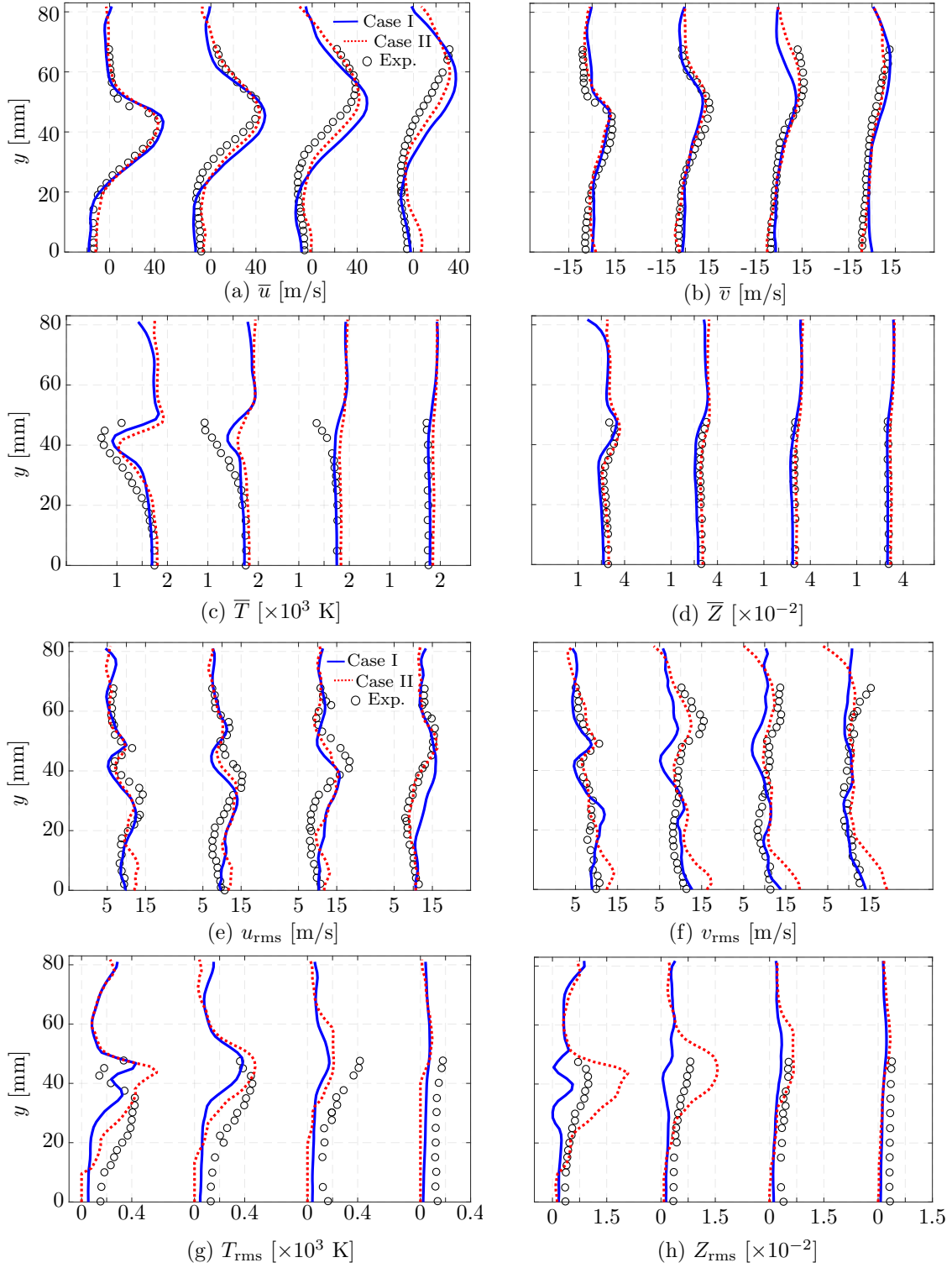
Figure 5. Vertical y-profiles of (a–d) mean and (e–h) rms flow variables at $\bar{p} = 3$ bar for four axial locations: $x = 18.7$, 38.7, 58.7 and 88.7 mm. Solid line: Case I with PaSR model; dotted line: Case II with PDF model; circle: experimental data (Bulat et al., 2014).
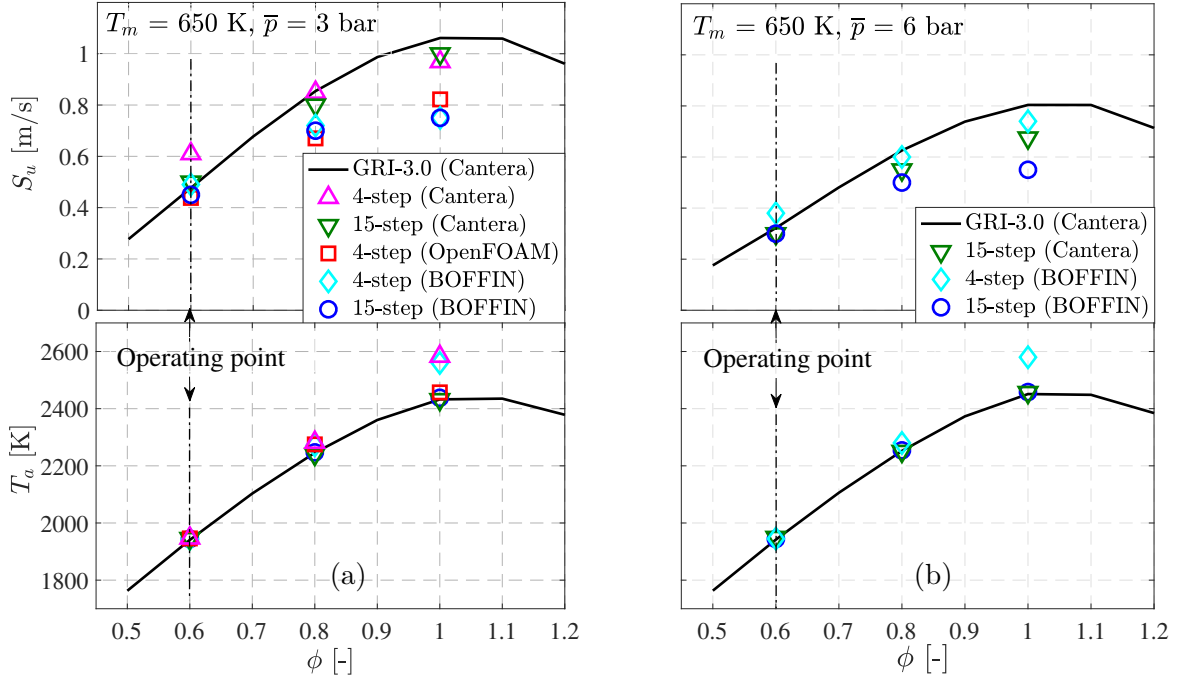
Figure 6. Laminar burning velocity (S_u) and adiabatic flame temperature (T_a) against equivalence ratio (ϕ) at (a) $\bar{p} = 3$ bar and (b) $\bar{p} = 6$ bar, both with an ambient temperature of $T_m = 650$ K. Solid line: Cantera with GRI-Mech 3.0; $\triangle$: Cantera with 4-step scheme; $\triangledown$: Cantera with 15-step scheme; $\square$: OpenFOAM with 4-step scheme; $\diamond$: BOFFIN with 4-step scheme; $\bigcirc$: BOFFIN with 15-step scheme. The operating point is $\phi = 0.6$.

4-step and 15-step schemes, especially at higher ϕ. These results are as anticipated given the constant Schmidt and Prandtl number assumption[2], as it is well known that this leads to an under-prediction of the burning velocity at higher equivalence ratios (Poinsot & Veynante, 2005). Nevertheless, the adiabatic flame temperature and burning velocity are correctly reproduced by both LES solvers at the combustor operating point of $\phi = 0.6$; discrepancies occur around stoichiometric equivalence ratios.

Following the above validation, the effect of reaction chemistry on the unforced LES is shown in Fig. 7, which compares Cases II and III using BOFFIN code. The impact of reaction scheme on the mean flow field is marginal, while the 4-step scheme gives a slightly shorter low temperature zone and a higher-magnitude heat release rate. This may be due to the slightly higher laminar burning velocity of the 4-step reaction with BOFFIN at $\phi = 0.6$ (Fig. 6(a)), which reduces the axial extent of the reaction zone and increases the fuel burnt at the flame,

---

[2]Recent computations of laminar flames with BOFFIN using accurate transport properties reproduce the GRI results.
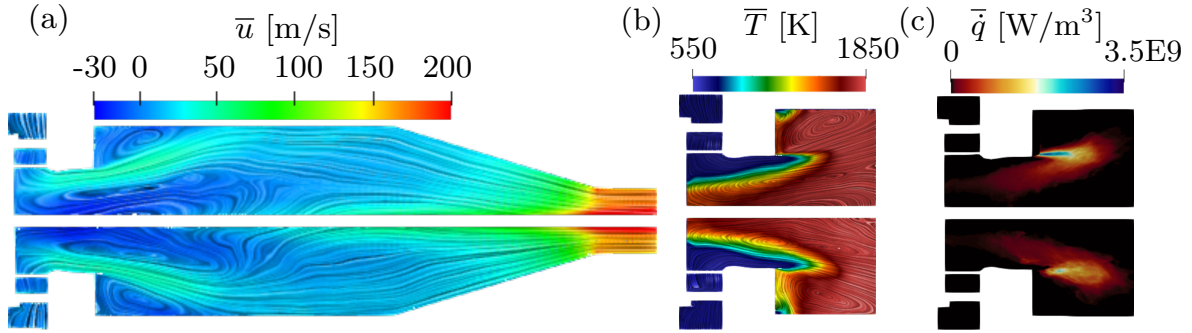
Figure 7. Time-averaged contours of (a) axial velocity, $\overline{u}$, (b) temperature, $\overline{T}$, and (c) volumetric heat release rate, $\overline{\overline{q}}$, computed at 3 bar by (top) Case II with 4-step scheme and (bottom) Case III with 15-step scheme.

thus leading to a higher heat release rate.

Figure 8 compares the vertical y-profiles of mean and rms variables between Cases II and III. The match between LES and experiments is generally good for all the variables at all locations, with errors within the limits of measurement uncertainties (Bulat et al., 2014), confirming both chemical schemes are accurate. The 4-step scheme slightly over-predicts the mean temperature, $\overline{T}$, and mass fraction of H_2O, but under-predicts the mass fraction of CH_4 compared to the 15-step scheme. These are consistent with the small differences in the predicted unforced flame (see Figs. 7(b, c)).

Finally, the effect of operating pressure on the unforced simulations is analysed. The burning velocity and temperature computed by the two simple schemes with BOFFIN are compared with GRI-Mech 3.0 at 6 bar pressure in Fig. 6(b). Increasing pressure globally reduces the laminar burning velocity for all equivalence ratios, but does not affect the adiabatic flame temperature, consistent with Poinsot and Veynante (2005). Both schemes correctly predict the burning velocity and temperature, with the errors against GRI-Mech 3.0 increasing with ϕ. Finally, the BOFFIN 4-step scheme gives a slightly higher burning velocity than the BOFFIN 15-step scheme, consistent with their predictions at 3 bar. Although the accurate transport properties used in Cantera improve the burning velocity prediction at high ϕ, the two simple BOFFIN schemes are both accurate enough for operation at $\phi = 0.6$.

Based on the above validation, the contours of mean flow variables are compared in Fig. 9

13
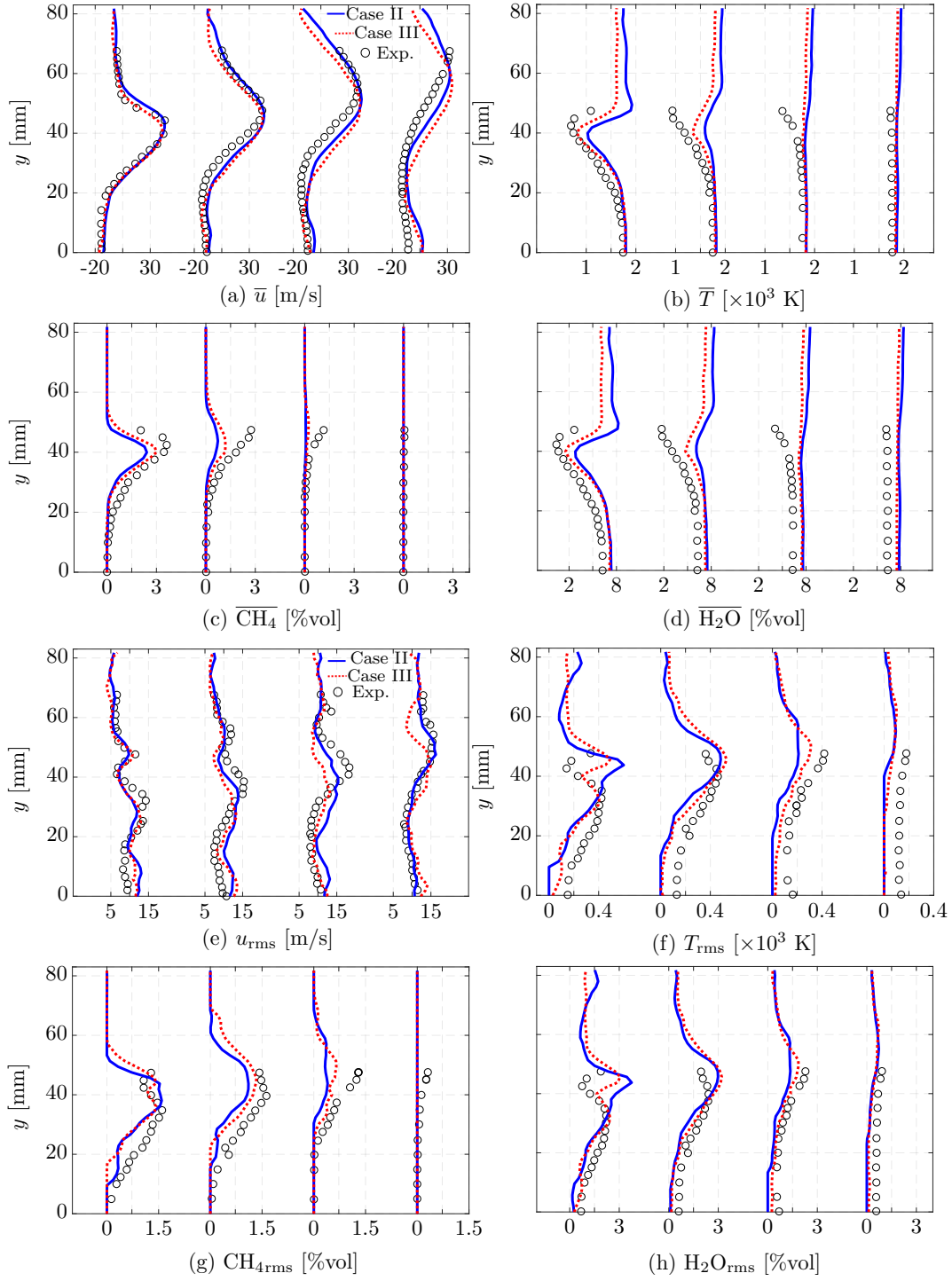
Figure 8. Vertical y-profiles of (a–d) mean and (e–h) rms flow variables at 3 bar. Solid line: Case II with 4-step scheme; dotted line: Case III with 15-step scheme; circle: Experimental data (Bulat et al., 2014).

between Cases IV and V. Both schemes yield similar mean velocity fields, indicating the small effect of reaction chemistry on the flow. Due to the faster burning velocity, the 4-step scheme gives a shorter low temperature zone and a higher flame heat release rate than the 15-step
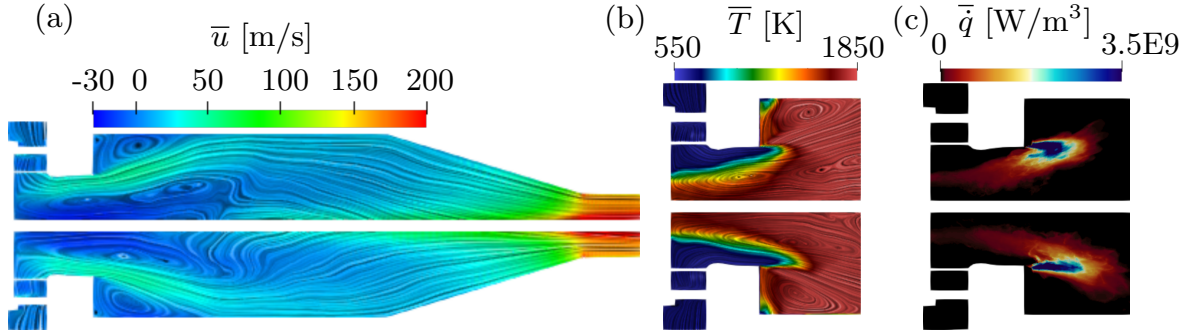
Figure 9. Time-averaged contours (a) axial velocity, $\overline{u}$, (b) temperature, $\overline{T}$, and (c) volumetric heat release rate, $\overline{\overline{q}}$, computed at 6 bar by (top) Case IV with 4-step scheme and (bottom) Case V with 15-step scheme.

chemistry. Compared to 3 bar predictions (Figs. 7(b, c)), the low temperature zone is much shorter at 6 bar for both schemes, while the heat release rate is now much higher. These differences between 3 bar and 6 bar simulations are mainly caused by the increase of mixture density associated with a higher pressure and correspondingly a higher chemical reaction rate.

The vertical profiles of 6 bar variables are shown in Fig. 10 for Cases IV and V. A larger deviation between the LES and experiments is now evident, especially for some rms variables (e.g., CH_{4rms}). This may be due to the fact that the combustor is stable at 3 bar, but becomes unstable at 6 bar with a large-amplitude limit cycle oscillation. Although the 4-step scheme is sufficiently accurate for the flow field, the more detailed 15-step scheme gives improved predictions for the temperature and species mass fractions, e.g., CH_4 and H_2O.

5. Flame Describing Functions

The forced flame heat release responses in the analysed combustor are now computed. The above simulated unforced flame is submitted to an upstream velocity perturbation, u_1, located at the main air inlet of the swirler entry, varying harmonically as:

$$u_1 = \overline{u}_1 \cdot [1 + A_u \sin (2\pi f_u t)], \tag{5}$$

with $\overline{u}_1 \simeq 5$ m/s the mean inflow velocity, f_u the perturbation frequency and $A_u = |u'_1/\overline{u}_1|$ the normalised perturbation amplitude. To construct the FDFs, two forcing amplitudes ($A_u = 0.1$
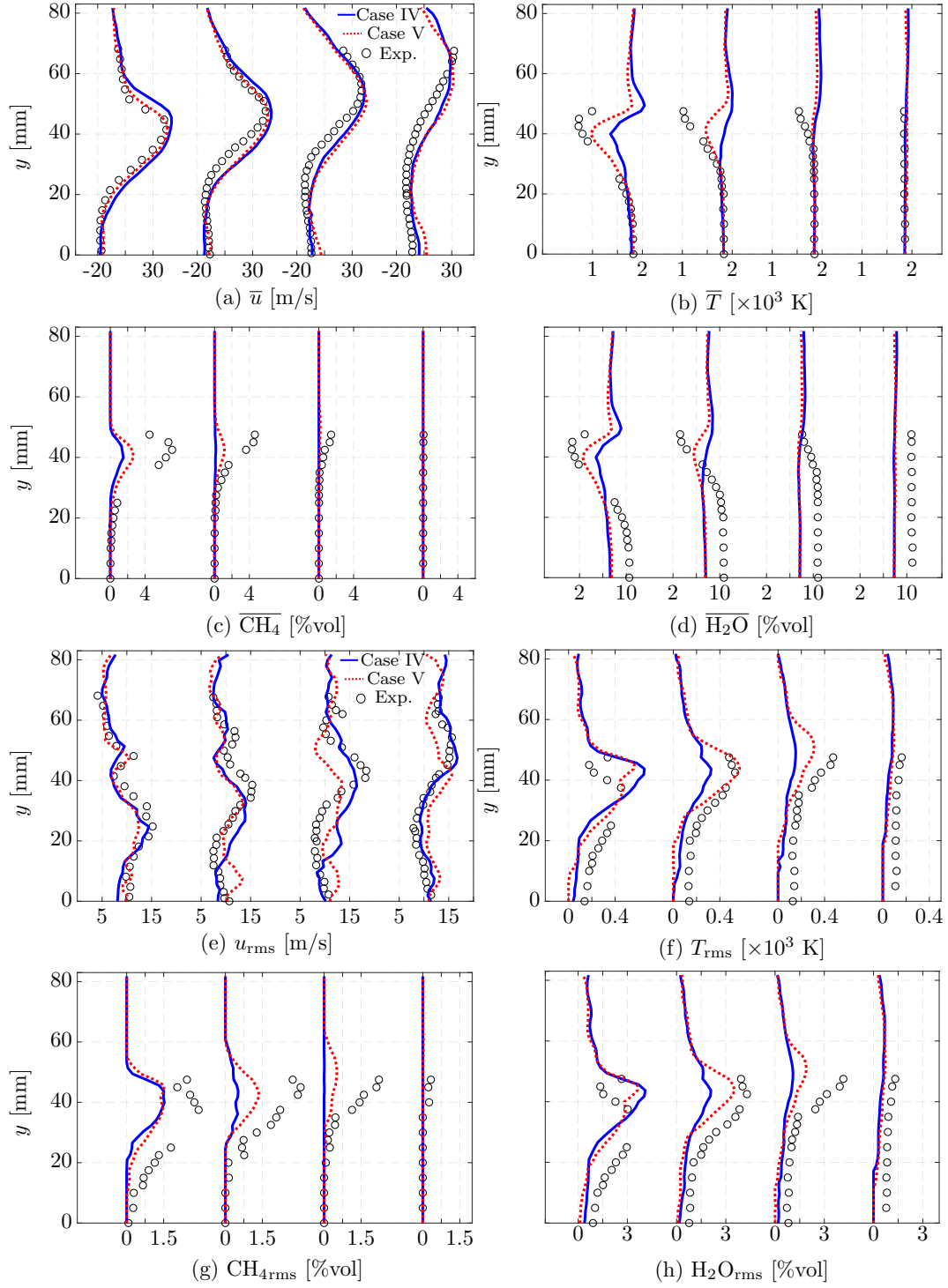
Figure 10. Vertical y-profiles of (a–d) mean and (e–h) rms flow variables at 6 bar. Solid line: Case IV with 4-step scheme; dotted line: Case V with 15-step scheme; circle: experimental data from DLR.

and 0.2) across eight forcing frequencies from 200 Hz to 1500 Hz are used. For each forcing

case, a time-period of at least 15 forcing cycles (after the initial transients vanish) has been

simulated. The convergence of the computed FDF properties (e.g., gain and phase) is usually achieved after 10 − 12 cycles. The gain, G, and phase, φ, of the resulting FDFs are plotted in Figs. 11− 15 for different LES cases. Some common trends are observed for all the FDFs:

(i) The FDF gain has two local maxima with a local minimum in between. The first maximum occurs at $f \simeq 200 − 300$ Hz, the gain minimum near $f = 600$ Hz and the second maximum at $f = 800$ Hz. These local gain extrema have previously been found for an atmospheric swirling combustor (Palies et al., 2010), and are caused by the constructive and destructive interactions between the imposed longitudinal perturbation and the azimuthal perturbations generated by the flow swirl. While at atmospheric pressure (Palies et al., 2010), the gain minimum falls almost to zero, the present FDFs have a less pronounced gain minimum with $G \simeq 0.5$ at $f = 600$ Hz.

(ii) The FDF phase decreases linearly with frequency, consistent with recent LES studies (Palies et al., 2010). This is because it mainly depends on the time delay between the perturbation and the flame response, which is inversely proportional to the mean flow velocity, $\overline{u}$, and is little affected by other factors. The dynamics in φ near the frequency of the local gain minimum are much less pronounced for this pressurised rig than at atmospheric pressure (Palies et al., 2010).

(iii) An increase of the forcing amplitude, A_u, always leads to a decrease in the FDF gain, especially at higher frequencies. This gain saturation is caused by the levelling-off of the heat release rate oscillations at higher perturbation levels, and is consistent with previous studies (Han & Morgans, 2015). The FDF phase, however, shows very little forcing amplitude dependence.

The simulated FDFs are compared between LES cases to evaluate the effects of combustion model, reaction chemistry and operating pressure. As shown in Fig. 11, the FDFs for Cases I and II are compared at forcing level $A_u = 0.1$. The trends of the gain, G, and phase, φ, both generally match well, other than for small gain mismatches at lower frequencies (e.g., 300 −
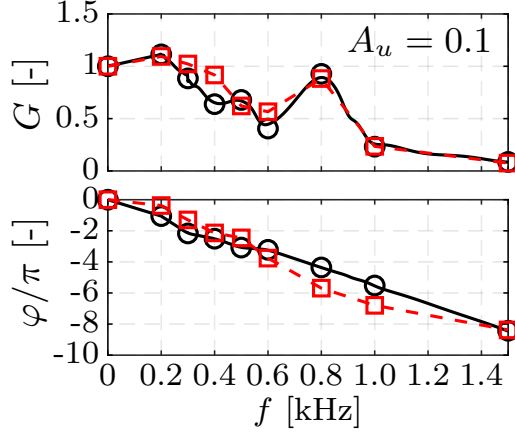
Figure 11. FDFs at $\bar{p} = 3$ bar for forcing amplitude $A_u = 0.1$, obtained for Case I with PaSR model (solid line with circles) and Case II with PDF model (dashed line with squares). (Top) gain G; (bottom) phase φ.
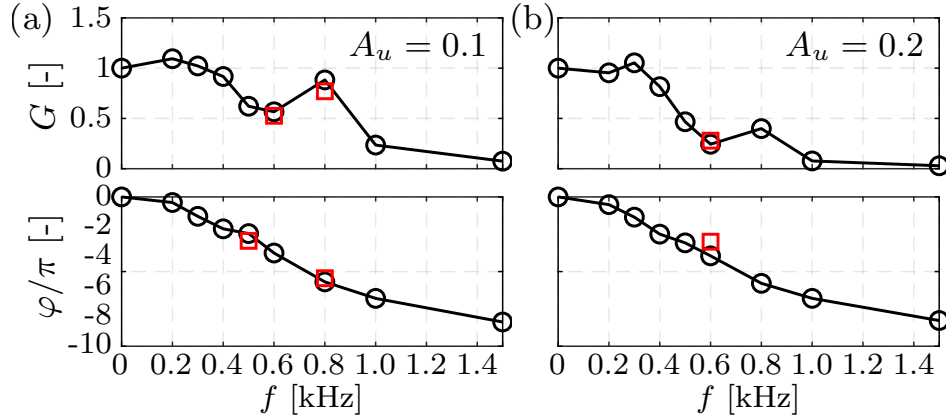

Figure 12. FDFs at $\bar{p} = 3$ bar, obtained for Case III with PDF model using one field (solid line with circles) and spot checks for 8 stochastic fields (squares). (Top) gain G; (bottom) phase φ. (a) $A_u = 0.1$; (b) $A_u = 0.2$.

600 Hz), likely caused by the higher heat release rate predicted by the PDF model (Fig. 4(c)). The effect of stochastic field number used by the PDF model is also studied based on Case III. The FDF gain and phase computed by 8 stochastic fields are shown in Fig. 12, and are very close to those obtained with only one field at both perturbation levels for two frequencies ($f_u = 600$ and 800 Hz). This implies that one field is sufficient for the PDF model to correctly capture the FDFs in the present combustor. Overall, the effect of sub-grid combustion model on the forced flame responses is relatively small.

Secondly, the effect of reaction chemistry on the FDFs is discussed. The FDFs obtained by Cases II and III are compared in Fig. 13. The magnitudes and trends of the gain and phase both match well for both forcing levels, with the gain's mismatch below 10%. This good match
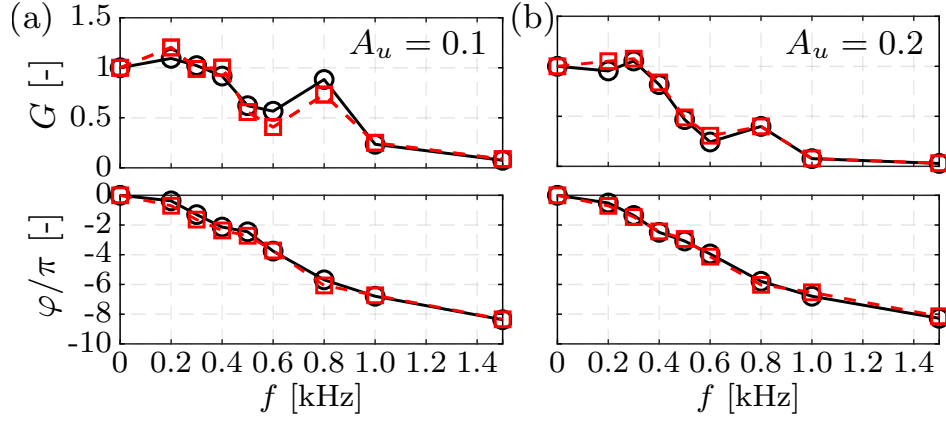
Figure 13. FDFs at $\bar{p} = 3$ bar for Case II with 4-step scheme (solid line with circles) and Case III with 15-step scheme (dashed line with squares). (Top) gain G; (bottom) phase φ. (a) $A_u = 0.1$; (b) $A_u = 0.2$.
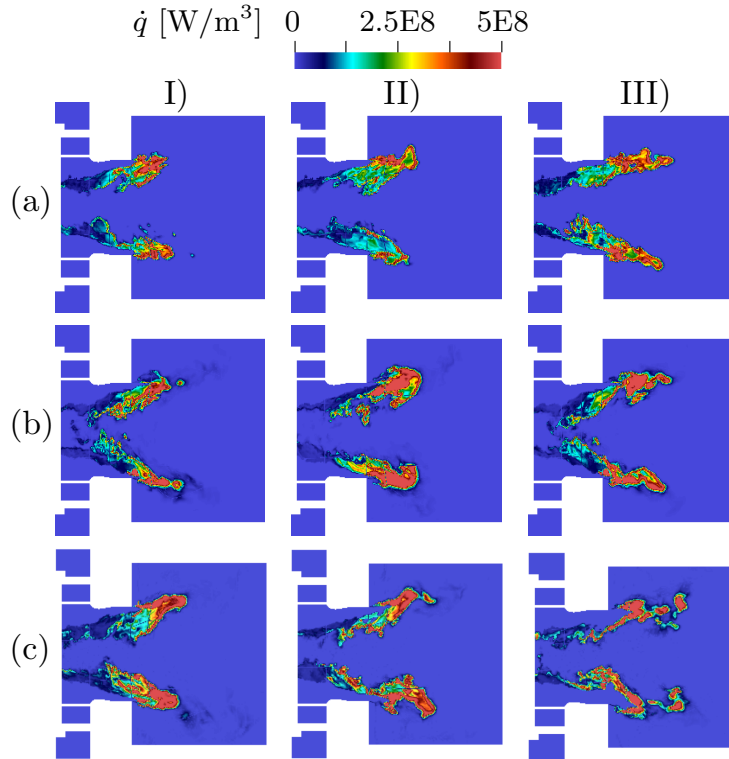

Figure 14. Snapshots of heat release rate field, $\dot{q}(x, y, z)$, on a symmetry plane, forced at $A_u = 0.1$, $f_u = 300$ Hz. (I) $\langle \dot{q} \rangle' / \overline{\langle \dot{q} \rangle}$ = -0.1; (II) $\langle \dot{q} \rangle' / \overline{\langle \dot{q} \rangle}$ = 0; (III) $\langle \dot{q} \rangle' / \overline{\langle \dot{q} \rangle}$ = 0.1. (a) Case II (4-step scheme, $\bar{p} = 3$ bar); (b) Case III (15-step scheme, $\bar{p} = 3$ bar); (c) Case V (15-step scheme, $\bar{p} = 6$ bar).

is also achieved at 6 bar. Although the mean flame shapes differ between the two reaction schemes at both pressures, with the more detailed 15-step scheme slightly more accurate, this difference barely affects the FDFs. The simpler 4-step scheme appears to be sufficient for FDF computation, this providing sufficient accuracy at reduced computational cost.

19

To further investigate the effect of reaction scheme, the unsteady flame dynamics of forced Cases II and III are compared in Fig. 14, choosing $f_u = 300$ Hz and $A_u = 0.1$ in order to achieve strong heat release oscillations. Three time snapshots of the heat release rate field, $\dot{q}(x, y, z)$, are compared within a forcing period, chosen to correspond to the normalised fluctuation, $\langle \dot{q} \rangle' / \overline{\langle \dot{q} \rangle}$, being minimum, zero and maximum (with $\langle \dot{q} \rangle = \iiint \dot{q} \mathrm{d}V$ and V the domain volume). Although the unforced flame shapes slightly differ between the two reaction schemes, the flame's oscillatory behaviour around its mean position is generally similar. The flame is shortest when $\langle \dot{q} \rangle' / \overline{\langle \dot{q} \rangle}$ is minimum, becoming longer when $\langle \dot{q} \rangle' = 0$, and being longest for the maximum of $\langle \dot{q} \rangle' / \overline{\langle \dot{q} \rangle}$. The heat release fluctuation is mainly associated with the variation in the flame surface area. Cases II (Fig. 14(a)) and III (Fig. 14(b)) show that a change in reaction scheme can modify the response of the flame structure, even at the same pressure. Although the more detailed 15-step scheme yields a slightly longer flame throughout the forcing period (Fig. 14(b)), consistent with the unforced flame in Fig. 7(c), differences in the detailed flame structure may still result in a similar flame surface area for the two reaction schemes, explaining the similarity in the FDF gains shown in Fig. 13.

Finally, the effect of operating pressure on the FDFs is analysed comparing Cases III and V. Figure 15(a) shows that at the lower forcing level, $A_u = 0.1$, increasing the pressure leads to an increase in FDF gain at lower frequencies ($f \leq 500$ Hz). This is in agreement with a recent experiment by Sabatino et al. (2018). The present FDF also exhibits a strong pressure-dependence of the frequency of its maximum gain: at 3 bar the maximum $G \simeq 1.2$ is found at $f = 200$ Hz, while at 6 bar it increases to $G \simeq 1.4$ and shifts to $f = 300$ Hz (Fig. 15(a)). This is not in agreement with Sabatino et al. (2018). In their work, a pressure increase from 1 bar to 4 bar does not vary the frequency of the maximum gain, with the change of gain level with pressure depending on the fuel used. They considered a different combustor geometry, flame shape and fuel type, etc., and their equivalence ratio was adjusted with pressure to ensure the same mean flame length for all pressures. In the present work, however, a fixed ϕ is used at both pressures, giving slightly different mean flame lengths, which may lead to
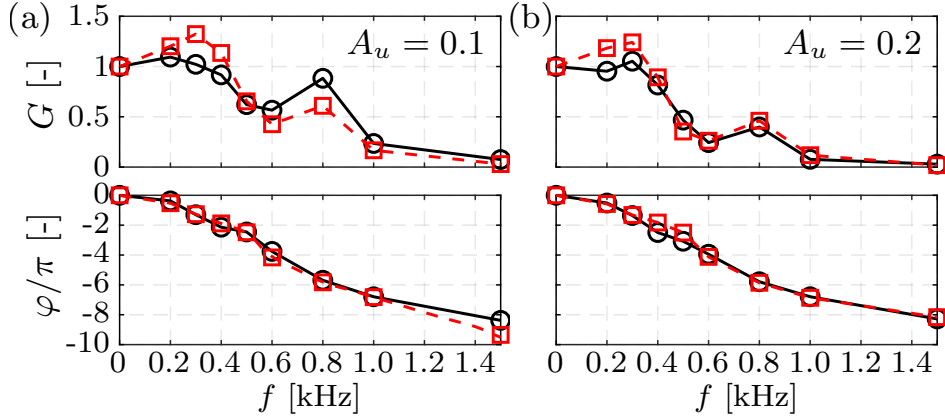
Figure 15. FDFs obtained for Case III at $\bar{p} = 3$ bar (solid line with circles) and Case V at $\bar{p} = 6$ bar (dashed line with squares), with (top) gain G and (bottom) phase φ. (a) $A_u = 0.1$; (b) $A_u = 0.2$.

different coupling between the flame and the imposed perturbation at two pressures, shifting the frequency of the maximum FDF gain.

At the higher forcing level of $A_u = 0.2$, the pressure dependence of the gain maximum is much weaker (Fig. 15(b)), mainly due to the stronger saturation of the flame surface oscillation at such high perturbations levels. For the FDF phase, the effect of the pressure is always negligible, consistent with the experiment (Sabatino et al., 2018).

Further insights into the pressure effect are provided by the flame dynamics for Cases III and V (see Figs. 14(b, c)). The predicted flame structures are similar, probably due to the same reaction scheme used. The flame surface area oscillation can be compared by examining the axial flame length. Increasing the pressure slightly increases the flame length, likely to be associated with the lower laminar burning velocity. The frequency dependence of the FDF gain with pressure in Fig. 15(a) can now be explained: the pressure increase gives a longer flame length and thus a longer flame response time. At lower frequencies (e.g., 300 Hz), the time-scale of the perturbation signal is also large, giving stronger coupling between the perturbation time and the response time. In contrast, at higher frequencies, the forcing period is much shorter, leading to a weaker coupling with the flame response and thus lower FDF gains.
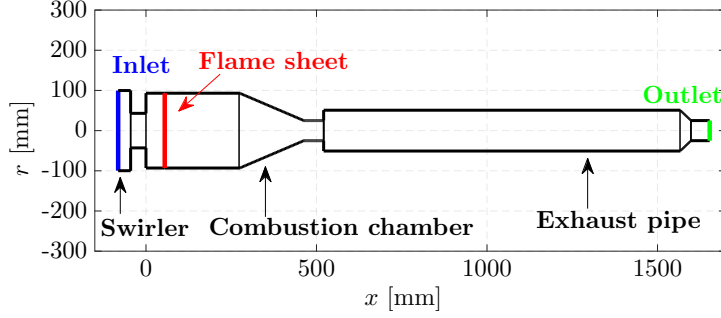
Figure 16. The simplified network model of the analysed combustor (Xia, Laera, et al., 2018).

6. Thermoacoustic Limit Cycle Prediction

In order to validate the above simulated FDFs, they are coupled with the low order network solver, OSCILOS (Li & Morgans, 2015), in order to predict the thermoacoustic stability of the analysed combustor. OSCILOS has been validated by experiments (Han et al., 2015). It represents the combustor geometry as a network of connected simple modules, as shown in Fig. 16. The length and cross-sectional area of each module match the original geometry and flow rates. The water spray section is neglected due to its large acoustic energy dissipation, and the upstream plenum is ignored as it is preferable to prescribe a physical acoustic boundary condition at the swirler inlet. The combustion chamber contraction is represented as a sequence of 50 constant area modules with successively decreasing areas. The mean flow is accounted for, with the mean flow variables assumed constant within each module, changing only between modules. The axial distributions of mean velocity and temperature in the network are reconstructed from the LES mean flow and the experimental data, respectively.

The acoustic waves are assumed linear and one-dimensional at the low frequencies of interest (Noiray et al., 2008). Thus within each module the acoustic perturbations satisfy the convected wave equation and can be represented as the sum of downstream and upstream travelling waves with different strengths. These wave strengths are tracked between modules using linearised flow conservation equations — these account for losses due to stagnation pressure drop at area expansions (Li et al., 2017). The boundary conditions for the network are defined by the pressure reflection coefficients, R, denoting the strength ratio of the re-

flected to incident acoustic waves at an end. In this work, the network inlet is assumed as highly-damped due to the perforated plate installed between the plenum and the swirler. The inlet reflection coefficient, R_{in}, is little affected by the operating pressure, and it increases in magnitude from $|R_{\mathrm{in}}| = 0$ to 0.15 and varies in phase between $\angle R_{\mathrm{in}} = $ -0.7π and -0.55π over frequency $f = 0 - 1000$ Hz. In contrast, the network outlet is defined as a slightly damped open end, which does not vary with pressure and has its magnitude $|R_{\mathrm{out}}|$ dropped from 1 to 0.91 and phase $\angle R_{\mathrm{out}}$ from π to 0.84π across 0 – 1000 Hz (Xia, Laera, et al., 2018).

Since the present flame has a much shorter axial extent ($\sim$100 mm) than the dominant acoustic wavelengths ($\sim$1–4 m), the flame zone is represented by an infinitely thin "flame sheet" at $x = 45$ mm, where the maximum mean heat release rate occurred in experiments (Stopper et al., 2013). The jump in acoustic wave strengths across the flame is accounted for using the linearised flow conservation equations across the flame sheet (Dowling, 1997). To account for the effect of acoustic waves on the flame response, a flame model is prescribed, in this work in the form of an FDF.

To predict the linear stability of the combustor, the thermoacoustic modes of the above network geometry are computed using FDFs at $A_u = 0.1$ for Cases III and V with 15-step scheme. The complex frequencies, $\omega = \sigma + i2\pi f$ (with σ the growth rate), for which both the inlet and outlet boundary conditions are satisfied, are identified within OSCILOS using a "shooting method" (Han et al., 2015). The computed modes are marked by white stars in Fig. 17, showing that all modes are predicted to be stable at 3 bar, while at 6 bar one mode at $f \simeq 231$ Hz is predicted to be unstable. The predicted stabilities match well with the experimental observations (Stopper et al., 2013; Xia, Morgans, Jones, Rogerson, et al., 2017), and are unchanged if the 4-step scheme FDFs (Cases II and IV) are used instead of the 15-step ones.

The reason for the stability change with pressure is now considered: thermoacoustic stability is governed by the combination of (i) acoustic waves and (ii) the flame response. For (i), the acoustic wave strength is determined by the geometry, speed of sound and boundary
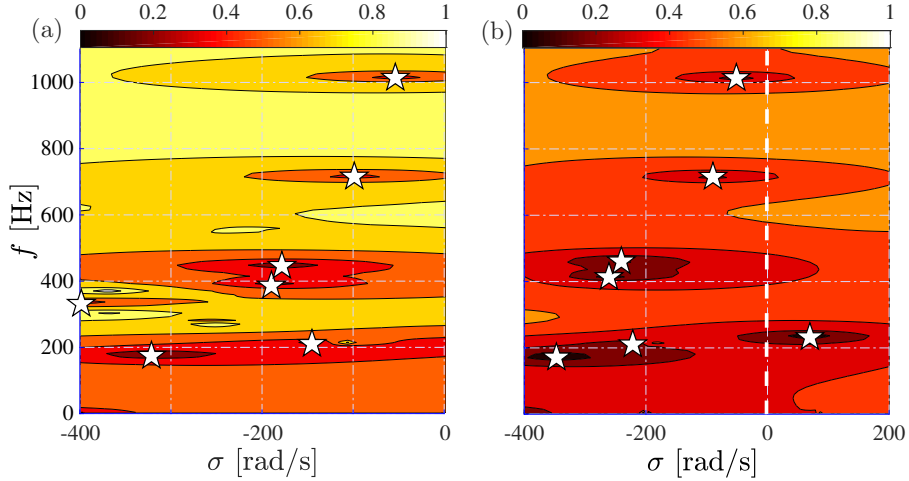
Figure 17. Linear stability maps of the analysed combustor at (a) 3 bar and (b) 6 bar pressure. The predicted thermoacoustic modes are marked by white stars on the complex $f - \sigma$ plane (Xia, Laera, et al., 2018).
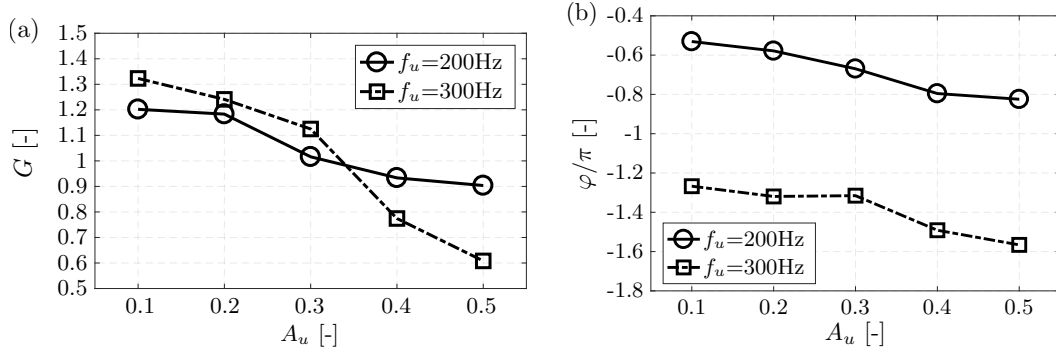

Figure 18. (a) Gain, G, and (b) phase, φ, of the FDF at $f_u = 200$ Hz (solid line) and 300 Hz (dash-dotted line) for perturbation levels of $A_u = 0.1 - 0.5$. All calculations performed at $\bar{p} = 6$ bar based on Case V (Xia, Laera, et al., 2018).

conditions, none of which are affected by the pressure in this work. Thus the flame response is the main source of the stability change. The FDF gain near the frequency of the unstable mode is higher at 6 bar than at 3 bar (Fig. 15(a)), mainly due to the reduced laminar burning velocity and increased flame length. The flame surface area oscillation and heat release fluctuation are subsequently enhanced for the longer flame at the higher pressure of 6 bar.

For the unstable mode, the final frequency and amplitude of the resulting limit cycle oscillations are now predicted. The 6 bar FDF of Case V (Fig. 15(a)) is extended from $A_u = 0.1$ to 0.5 (with steps of 0.1), for frequencies 200 Hz and 300 Hz, these falling on either side of the instability frequency. The flame response against forcing level is shown in Fig. 18. The FDF gain falls off with A_u at both frequencies with different trends. A stronger saturation
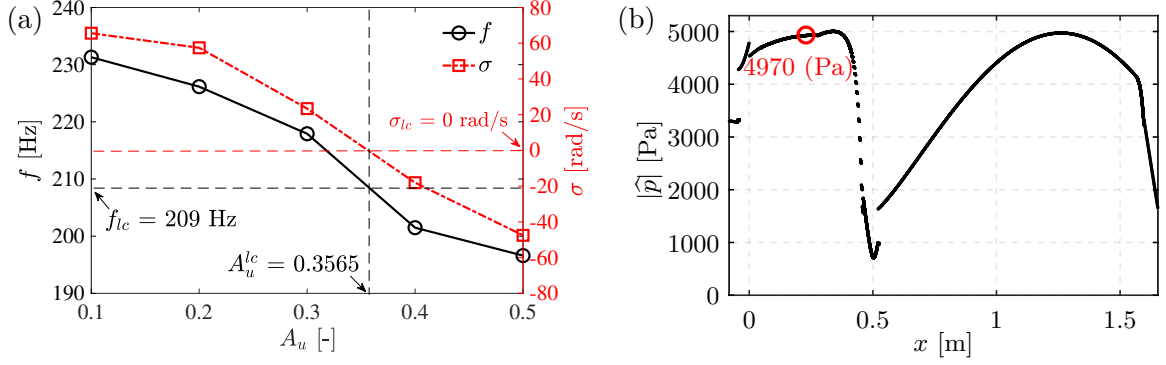
Figure 19. (a) Evolutions of frequency (f, solid line) and growth rate (σ, dash-dotted line) of the unstable mode with A_u. Arrows indicate the frequency, f_{lc}, and growth rate, σ_{lc}, of the limit cycle and the corresponding forcing level, A_u^{lc}. (b) Axial distribution of pressure fluctuation amplitude, $|\widehat{p}|$, when the limit cycle occurs. Circle refers to the $|\widehat{p}|$ value at the measurement location, $x = 0.231$ m (Xia, Laera, et al., 2018).

occurs at 300 Hz, with the gain dropping by more than 50% as A_u increases from 0.1 to 0.5. The gain drop at 200 Hz is $\sim$25%. This frequency dependence of the rate of the gain's fall-off with forcing level has been observed in previous numerical (Han et al., 2015) and experimental (Noiray et al., 2008) studies. The FDF phase shows an almost linearly-decreasing trend with forcing level at both frequencies.

This extended FDF is then coupled with OSCILOS to predict the limit cycle frequency and amplitude. This nonlinear prediction relies on the assumption that the time-scale over which the oscillation amplitude grows is much longer than that of the oscillation itself (Laera et al., 2017). The frequencies and growth rates of the thermoacoustic oscillations are predicted across forcing levels, with the zero-growth-rate state taken to correspond to that at which the limit cycle establishes (Noiray et al., 2008; Han et al., 2015; Laera & Camporeale, 2017).

The evolutions of frequency, f, and growth rate, σ, of the linearly unstable mode are shown in Fig. 19(a) over forcing level. Using linear interpolation, the limit cycle perturbation level is $A_u^{lc} = 0.3565$, with a frequency of $f_{lc} = 209$ Hz. The latter is very close to the measured value of 216 Hz (Fig. 2(b)). The axial distribution of the pressure fluctuation amplitude, $|\widehat{p}|\,(x)$, under a limit cycle is shown in Fig. 19(b). At the location where the pressure signal was measured, $x = 231$ mm, a fluctuation amplitude of $|\widehat{p}_{lc}| = 4970$ Pa is predicted, close to the measured value of 5000 Pa (Fig. 2(b)). The same predictions are repeated with 4-step chemistry FDFs

25

(Case IV), giving $f_{lc} = 211$ Hz, $A_u^{lc} = 0.3559$ and $|\hat{p}| = 4940$ Pa, again very close to the experimental data. In light of this accurate limit cycle prediction, the above simulated FDFs can be considered validated.

The thermoacoustic stabilities and limit cycle predictions are known to be sensitive to the acoustic boundary conditions, which for the present combustor are unknown as they were not measured. We therefore investigate the sensitivity of the above predictions (with 15-step FDFs) to small changes in the upstream and downstream acoustic boundary conditions. If R_{in} is taken to have its gain changed by 10% either way, with the outlet reflection coefficient unchanged, the predictions change to $f_{lc} = 210$ Hz, $A_u^{lc} = 0.3557$ and $|\hat{p}| = 4947$ Pa (for 10% decrease) and $f_{lc} = 209$ Hz, $A_u^{lc} = 0.3574$ and $|\hat{p}| = 4993$ Pa (for 10% increase). Similarly, if R_{out} is rather to have its gain changed by 10% either way, with the inlet reflection coefficient unchanged, the predictions change to $f_{lc} = 205$ Hz, $A_u^{lc} = 0.3825$ and $|\hat{p}| = 5280$ Pa (for 10% decrease) and $f_{lc} = 214$ Hz, $A_u^{lc} = 0.3358$ and $|\hat{p}| = 4715$ Pa (for 10% increase). Hence, the predicted limit cycle has a very small dependence on the inlet reflection coefficient, although it is more sensitive to the change of outlet reflection coefficient. An increase of $|R_{in}|$ or decrease of $|R_{out}|$ are both found to reduce the value of f_{lc} but increase A_u^{lc} and $|\hat{p}|$.

7. Conclusions

This work simulates the responses of a turbulent swirling flame to upstream perturbation in a pressurised gas turbine combustor, and used them to construct the weakly nonlinear flame describing functions (FDFs). Two incompressible LES solvers are used, applying two sub-grid combustion models (PaSR and PDF) and two reaction schemes (4-step and 15-step) at two operating pressures (3 bar and 6 bar). It is found that (i) the mean flow is not affected by these factors; (ii) the PaSR model and the 15-step scheme both give a longer flame with a lower heat release rate, although due to different reasons; (iii) an increase in the pressure leads to a higher mean heat release rate. Both combustion models and the used reaction schemes

offer good accuracy for the unforced flow and flame.

The flame responses to an upstream harmonic velocity perturbation are then computed across several perturbation frequencies and amplitudes. The constructed FDFs have some common trends: (i) the FDF gain has two local maxima with one local minimum in between; (ii) the FDF phase linearly decreases with frequency; (iii) an increase in the perturbation level always reduces the gain. For a given pressure, the combustion model and reaction scheme both have very small effects on the FDFs, regardless of the differences in the predicted unforced flame. The faster 4-step scheme is thus recommended for FDF computation. A pressure increase leads to an increase in FDF gain at low frequencies but to a drop at higher frequencies.

The simulated FDFs are finally validated by performing thermoacoustic predictions using the low order network approach. The combustor is predicted linearly stable at 3 bar, but unstable at 6 bar near $\sim$231 Hz, both in agreement with the experimental data. Based on the unstable mode, the limit cycle is predicted to occur at frequency 209 Hz with a pressure amplitude of 4970 Pa, both matching the measured data of 216 Hz and 5000 Pa. The sensitivity of the predicted limit cycle to the acoustic boundary conditions is also discussed.

References

Abou-Taouk, A., Farcy, B., Domingo, P., Vervisch, L., Sadasivuni, S., & Eriksson, L. E. (2016). Optimized reduced chemistry and molecular transport for large eddy simulation of partially premixed combustion in a gas turbine. *Combust. Sci. Technol.*, **188**, 21–39.

Bauerheim, M., Staffelbach, G., Worth, N. A., Dawson, J., Gicquel, L. Y., & Poinsot, T. (2015). Sensitivity of LES-based harmonic flame response model for turbulent swirled flames and impact on the stability of azimuthal modes. *Proc. Combust. Instit.*, **35**(3), 3355–3363.

Boström, E. (2015). *Investigation of outflow boundary conditions for convection-dominated incompressible fluid flows in a spectral element framework* (Master's thesis). SCI School of Engineering Sciences, KTH Royal Institute of Technology, Stockholm, Sweden. (https://www.diva-portal.org/smash/get/diva2:804993/FULLTEXT01.pdf)

Bulat, G. (2012). *Large eddy simulations of reacting swirling flows in an industrial burner* (Doctoral dissertation). Imperial College London, London.

Bulat, G., Jones, W. P., & Marquis, A. J. (2014). NO and CO formation in an industrial gas-turbine combustion chamber using LES with the Eulerian sub-grid PDF method. *Combust. Flame*, **161**(7), 1804–1825.

Bulat, G., Jones, W. P., & Navarro-Martinez, S. (2015). Large eddy simulations of isothermal confined swirling flow in an industrial gas-turbine. *Int. J. Heat Fluid Fl.*, **51**, 50–64.

Chomiak, J., & Karlsson, A. (1996). Flame liftoff in diesel sprays. *Symp. (Int.) Combust.*, **26**(2), 2557–2564.

Dowling, A. P. (1997). Nonlinear self-excited oscillations of a ducted flame. *J. Fluid Mech.*, **346**, 271–290.

Febrer, G., Yang, Z., & McGuirk, J. (2011). A hybrid approach for coupling of acoustic wave effects and incompressible LES of reacting flows. *The 47th AIAA/ASME/SAE/ASEE Joint Propulsion Conference & Exhibit*, Paper No. AIAA 2011-6127.

Fedina, E., Fureby, C., Bulat, G., & Meier, W. (2017). Assessment of finite rate chemistry large eddy simulation combustion models. *Flow, Turb. Combust.*, **99**(2), 385–409.

Fureby, C., Nordin-Bates, K., Petterson, K., Bresson, A., & Sabelnikov, V. (2015). A computational study of supersonic combustion in strut injector and hypermixer flow fields. *Proc. Combust. Instit.*, **35**(2), 2127–2135.

Goodwin, D. G., Moffat, H. K., & Speth, R. L. (2014). *Cantera: an object-oriented software toolkit for chemical kinetics, thermodynamics, and transport processes.* `http://www.cantera.org`. (Version 2.1.2)

Gregory, P. S., Golden, D. M., Frenklach, M., Moriarty, N. W., Eiteneer, B., Goldenberg, M., ... Qin, Z. (2018). *GRI-Mech 3.0* (Tech. Rep.). UC Berkeley. (http://combustion.berkeley.edu/gri-mech/)

Han, X., Laera, D., Morgans, A. S., Sung, C. J., Hui, X., & Lin, Y. Z. (2018). Flame macrostructures and thermoacoustic instabilities in stratified swirling flames. *Proc. Comb. Inst.*, in press - https://doi.org/10.1016/j.proci.2018.06.147.

Han, X., Li, J., & Morgans, A. S. (2015). Prediction of combustion instability limit cycle oscillations by combining flame describing function simulations with a thermoacoustic network model. *Combust. Flame*, **162**(10), 3632–3647.

Han, X., & Morgans, A. S. (2015). Simulation of the flame describing function of a turbulent premixed flame using an open-source LES solver. *Combust. Flame*, **162**(5), 1778–1792.

Hermeth, S., Staffelbach, G., Gicquel, L. Y., Anisimov, V., Cirigliano, C., & Poinsot, T. (2014). Bistable swirled flames and influence on flame transfer functions. *Combust. Flame*, **161**(1), 184–196.

Jones, W. P., Marquis, A. J., & Prasad, V. N. (2012). LES of a turbulent premixed swirl burner using the Eulerian stochastic field method. *Combust. Flame*, **159**(10), 3079–3095.

Jones, W. P., & Navarro-Martinez, S. (2007, August). Large eddy simulation of autoignition with a subgrid probability density function method. *Combust. Flame*, **150**(3), 170-187.

Jones, W. P., & Prasad, V. N. (2010). Large eddy simulation of the Sandia flame series (D, E and F) using the Eulerian stochastic field method. *Combust. Flame*, **157**, 1621-1636.

Krediet, H., Beck, C., Krebs, W., & Kok, J. (2013). Saturation mechanism of the heat release

response of a premixed swirl flame using LES. *Proc. Combust. Instit.*, **34**(1), 1223–1230.

Laera, D., Campa, G., & Camporeale, S. M. (2017). A finite element method for a weakly nonlinear dynamic analysis and bifurcation tracking of thermo-acoustic instability in longitudinal and annular combustors. *Appl. Energy*, *187*, 216–227.

Laera, D., & Camporeale, S. M. (2017). A weakly nonlinear approach based on a distributed flame describing function to study the combustion dynamics of a full-scale lean-premixed swirled burner. *J. Eng. Gas Turb. Power*, *139*(9), 091501.

Lee, C. Y., & Cant, S. (2017). LES of nonlinear saturation in forced turbulent premixed flames. *Flow Turb. Combust.*, **99**(2), 461–486.

Li, J., & Morgans, A. S. (2015). Time domain simulations of nonlinear thermoacoustic behaviour in a simple combustor using a wave-based approach. *J. Sound Vib.*, **346**, 345–360.

Li, J., Xia, Y., Morgans, A. S., & Han, X. (2017). Numerical prediction of combustion instability limit cycle oscillations for a combustor with a long flame. *Combust. Flame*, **185**, 28–43.

National Institute of Standards and Technology (NIST). (1998). *NIST-JANAF Thermochemical Tables (4th ed.).* NIST Standard Reference Database 13, NIST, U. S. Department of Commerce. (https://dx.doi.org/10.18434/T42S31)

Noiray, N., Durox, D., Schuller, T., & Candel, S. (2008). A unified framework for nonlinear combustion instability analysis based on the flame describing function. *J. Fluid Mech.*, **615**, 139–167.

Palies, P., Durox, D., Schuller, T., & Candel, S. (2010). The combined dynamics of swirler and turbulent premixed swirling flames. *Combust. Flame*, **157**(9), 1698–1717.

Piomelli, U., & Liu, J. (1995). Large-eddy simulation of rotating channel flows using a localized dynamic model. *Phys. Fluids*, **7**(4), 839–848.

Poinsot, T., & Veynante, D. (2005). *Theoretical and numerical combustion (2nd ed.).* RT Edwards, Inc., Philadelphia, PA, USA. p.34.

Sabatino, F. D., Guiberti, T. F., Boyette, W. R., Roberts, W. L., Moeck, J. P., & Lacoste, D. A. (2018). Effect of pressure on the transfer functions of premixed methane and propane swirl flames. *Combust. Flame*, **193**, 272-282.

Sabelnikov, V., & Fureby, C. (2013). LES combustion modeling for high Re flames using a multi-phase analogy. *Combust. Flame*, **160**(1), 83–96.

Stopper, U., Aigner, M., Ax, H., Meier, W., Sadanandan, R., Stöhr, M., & Bonaldo, A. (2010). PIV, 2D-LIF and 1D-Raman measurements of flow field, composition and temperature in premixed gas turbine flames. *Exp. Therm Fluid Sci.*, **34**(3), 396–403.

Stopper, U., Meier, W., Sadanandan, R., Stöhr, M., Aigner, M., & Bulat, G. (2013). Experimental study of industrial gas turbine flames including quantification of pressure influence on flow field, fuel/air premixing and flame shape. *Combust. Flame*, **160**(10), 2103–2118.

Sung, C. J., Law, C. K., & Chen, J.-Y. (2001). Augmented reduced mechanisms for NO emission in methane oxidation. *Combust. Flame*, **125**(1), 906–919.

Sweby, P. K. (1984). High resolution schemes using flux limiters for hyperbolic conservation laws. *SIAM J. Numer. Anal.*, **21**(5), 995–1011.

Weller, H. G., Tabor, G., Jasak, H., & Fureby, C. (1998). A tensorial approach to computational continuum mechanics using object-oriented techniques. *Comput. Phys.*, **12**(6), 620–631.

Xia, Y., Duran, I., Morgans, A. S., & Han, X. (2016). Dispersion of entropy waves advecting through combustor chambers. *Proceedings of the 23rd International Congress on Sound & Vibration (ICSV23),* Athens, Greece.

Xia, Y., Duran, I., Morgans, A. S., & Han, X. (2018). Dispersion of entropy perturbations transporting through an industrial gas turbine combustor. *Flow, Turb. Combust.*, **100**(2), 481–502.

Xia, Y., Laera, D., Morgans, A. S., Jones, W. P., & Rogerson, J. W. (2018). Thermoacoustic limit cycle predictions of a pressurised longitudinal industrial gas turbine combustor. *ASME Turbo Expo*, Paper No. GT2018-75146.

Xia, Y., Li, J., Morgans, A. S., & Han, X. (2017). Computation of local flame describing functions for thermoacoustic oscillations in a combustor with a long flame. *Proceedings of the 8th European Combustion Meeting (ECM8),* Dubrovnik, Croatia.

Xia, Y., Morgans, A. S., Jones, W. P., & Han, X. (2017). Simulating flame response to acoustic excitation for an industrial gas turbine combustor. *Proceedings of the 24th International Congress on Sound & Vibration (ICSV24),* London, UK.

Xia, Y., Morgans, A. S., Jones, W. P., Rogerson, J. W., Bulat, G., & Han, X. (2017). Predicting thermoacoustic instability in an industrial gas turbine combustor: combining a low order network model with flame LES. *ASME Turbo Expo*, Paper No. GT2017-63247.